In Vivo Quantification of Human Serotonin 1A Receptor Using ^{11}C-CUMI-101, an Agonist PET Radiotracer

Matthew S. Milak[1,2], Christine DeLorenzo[1], Francesca Zanderigo[2], Jaya Prabhakaran[1], J.S. Dileep Kumar[1,2], Vattoly J. Majo[1], J. John Mann[1–3], and Ramin V. Parsey[1,2]

[1]Department of Psychiatry, Columbia University College of Physicians and Surgeons, New York, New York; [2]Department of Molecular Imaging, New York State Psychiatric Institute, New York, New York; and [3]Department of Radiology, Columbia University College of Physicians and Surgeons, New York, New York

The serotonin (5-hydroxytryptamine, or 5-HT) type 1A receptor (5-HT_{1A}R) is implicated in the pathophysiology of numerous neuropsychiatric disorders. We have published the initial evaluation and reproducibility *in vivo* of [*O*-methyl-^{11}*C*]2-(4-(4-(2-methoxyphenyl)piperazin-1-yl)butyl)-4-methyl-1,2,4-triazine-3,5(2*H*,4*H*)dione (^{11}C-CUMI-101), a novel 5-HT_{1A} agonist radiotracer, in *Papio anubis*. Here, we report the optimal modeling parameters of ^{11}C-CUMI-101 for human PET studies. **Methods:** PET scans were obtained for 7 adult human volunteers. ^{11}C-CUMI-101 was injected as an intravenous bolus, and emission data were collected for 120 min in 3-dimensional mode. We evaluated 10 different models using metabolite-corrected arterial input functions or reference region approaches and several outcome measures. **Results:** When using binding potential ($BP_F = B_{avail}/K_D$ [total available receptor concentration divided by the equilibrium dissociation constant]) as the outcome measure, the likelihood estimation in the graphical analysis (LEGA) model performed slightly better than the other methods evaluated at full scan duration. The average test–retest percentage difference was 9.90% ± 5.60%. When using BP_{ND} ($BP_{ND} = f_{nd} \times B_{avail}/K_D$; BP_{ND} equals the product of BP_F and f_{nd} [free fraction in the nondisplaceable compartment]), the simplified reference tissue method (SRTM) achieved the lowest percentage difference and smallest bias when compared with nondisplaceable binding potential obtained from LEGA using the metabolite-corrected plasma input function ($r^2 = 0.99$; slope = 0.92). The time–stability analysis indicates that a 120-min scan is sufficient for the stable estimation of outcome measures. Voxel results were comparable to region-of-interest–based analysis, with higher spatial resolution. **Conclusion:** On the basis of its measurable and stable free fraction, high affinity and selectivity, good blood–brain barrier permeability, and plasma and brain kinetics, ^{11}C-CUMI-101 is suitable for the imaging of high-affinity 5-HT_{1A} binding in humans.

Key Words: test–retest reproducibility; kinetic; compartment; voxel; bootstrap

J Nucl Med 2010; 51:1892–1900
DOI: 10.2967/jnumed.110.076257

The serotonergic system and the serotonin (5-hydroxytryptamine, or 5-HT) type 1A receptor (5-HT_{1A}R) are implicated in psychiatric disorders and the action of antidepressants (*1–8*). Positron emission tomography (PET) radiotracers allow *in vivo* quantification of 5-HT_{1A}R binding.

G-protein–coupled receptors exist in a high-agonist-affinity state that is bound to G-proteins and a low-affinity state (uncoupled from G-protein) (*9,10*). Antagonists bind to either state with equal affinity, and existing PET radiotracers for this receptor are antagonists. Additionally, agonist radiotracers are more likely to be sensitive to changes in intrasynaptic concentrations of the neurotransmitter (*11*), as demonstrated in the dopaminergic system (*12*). [*O*-methyl-^{11}C]2-(4-(4-(2-methoxyphenyl)piperazin-1-yl)butyl)-4-methyl-1,2,4-triazine-3,5(2*H*,4*H*)dione (^{11}C-CUMI-101), a new agonist radioligand (*13*), has a measurable free fraction and highly reproducible binding potential (BP_F) in *Papio anubis* (*14*).

We evaluate several modeling methods for quantifying ^{11}C-CUMI-101 binding in humans using a test–retest paradigm. We consider estimation of BP_F (B_{avail}/K_D [total available receptor concentration divided by the equilibrium dissociation constant]), the closest approximation to B_{avail}, at 6 different scanning durations.

MATERIALS AND METHODS

The study was approved by the Institutional Review Board, and participants gave written informed consent. Ten healthy volunteers signed an informed consent form, and 7 (3 women, 4 men; mean age ± SD, 32 ± 7 y) completed the study and were included in the analysis.

Radiochemistry

^{11}C-CUMI-101 was synthesized as previously described (*13,14*). The chemical purity of ^{11}C-CUMI-101 was 99.4% ± 2.3%, and the radiochemical purity was 99.4% ± 0.6%.

PET Studies

The PET procedure is described elsewhere (*15–17*). Polyurethane head molds minimized motion (Soule Medical). An ECAT HR+ scanner was used (Siemens/CTI). ^{11}C-CUMI-101 was injected over 30 s (384.84 ± 137.12 MBq [10.4 ± 3.7 mCi], with a mean specific activity of 33.54 ± 10.36 GBq/mmol [0.91 ± 0.28 mCi/nmol]). The average injected mass was 4.26 ± 0.68 μg.

Received Feb. 10, 2010; revision accepted Sep. 7, 2010.
For correspondence or reprints contact: Matthew S. Milak, Columbia University College of Physicians and Surgeons, 1051 Riverside Dr., Unit 42, New York, NY 10032.
E-mail: mm2354@columbia.edu

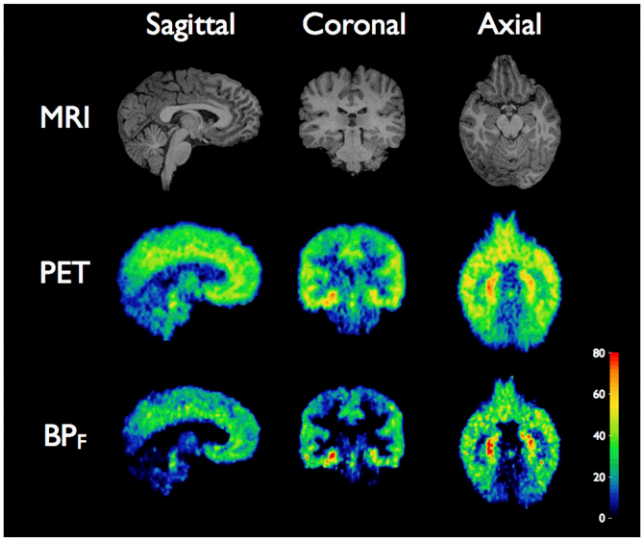

FIGURE 1. ^{11}C-CUMI binding. (Top) MR images of subject. (Middle) Sum of last 60 min (6 frames) of PET acquisition. (Bottom) BP_F value of every voxel within brain slices (calculated using EBEGA), with color bar indicating values of BP_F data shown.

Fourteen brain regions were evaluated. Correlations between injected mass and volume of distribution (V_T) ranged from −0.21 to 0.38 (*P* values ranged from 0.18 to 0.92). Emission data were collected in 3-dimensional mode for 120 min using 21 frames of increasing duration (3 × 20 s, 3 × 1 min, 3 × 2 min, 2 × 5 min, 10 × 10 min).

Input Function Measurement

The measurement of input function has been described elsewhere (*15–17*). Briefly, arterial samples were collected every 10 s in the first 2 min and less frequently thereafter, centrifuged, and plasma-separated. After initial extraction, the percentage of ^{11}C-CUMI-101 radioactivity in plasma was determined by high-performance liquid chromatography (*13*). These fractions were then plotted and fit with a Hill's function (*18*). The product of the unmetabolized fraction and the total plasma counts was fit with a second-order polynomial from time zero to the plasma peak and the sum of 3 exponentials from the peak to the end. The mean free fraction (*16*) was 0.30 ± 0.03.

Image Analysis

Using a 3-T Signa HDx system (GE Healthcare), we acquired T1-weighted MR images (3-dimensional fast spoiled gradient-recalled echo) for coregistration with PET images and identified regions of interest (ROIs) (*17*). Subject motion was corrected by coregistering each PET frame to frame 8, using FLIRT (FMRIB linear image registration tool, version 5.0; FMRIB Image Analysis Group). After attenuation correction, PET-to-MRI transformations were computed using FLIRT with a mutual information cost function and 6 degrees of freedom. Eight different coregistration possibilities, with varying source or target images and weighting masks, were performed, as previously described (*19*). The optimum transformation was applied to the average PET image and all PET frames. Images were resliced in FLIRT with trilinear interpolation, and the results were verified by visual inspection.

Automatic ROIs were obtained for all regions except the raphe, which was manually drawn on the subject's PET image. The algorithm assigns probabilistic ROIs to an MR image using an automated multilabel approach, in which the ROIs from each of 18 templates, after being gray-matter–masked, are nonlinearly transformed to the MR image. The 18 templates were created using 18 healthy subjects' MRI brain scans. ROIs were hand-drawn on each template MR image by experienced technicians trained to reliably approximate these regions using brain atlases (*20,21*) and published reports (*22,23*). Before the templates were applied to study subjects, each subject's MR image was preprocessed with Freesurfer (http://surfer.nmr.mgh.harvard.edu/), and the bias-corrected and intensity-normalized results were used in conjunction with gray matter, white matter, and cerebrospinal fluid maps derived with SPM5 (Wellcome Department of Cognitive Neurology) to remove nonbrain areas. Each of the 18 template MR images was then nonlinearly registered with the Automated Registration

TABLE 1
Metrics on High-Binding ROIs Using 120-Minute Scan and LEGA

ROI	Average BP_F of each ROI (mL/cm^3)	PD (%)	WSMSS (mL/cm^3)	ICC (unitless)	SD (%)	Identifiability (mL/cm^3)
Entorhinal cortex*	32.62	3.86 ± 12.42	6.32	0.87	20.79	4.68
Hippocampus	31.66	6.85 ± 5.98	3.90	0.90	18.86	4.70
Insula	28.61	5.44 ± 11.42	5.50	0.64	13.27	3.42
Posterior parahippocampal gyrus*	26.10	2.37 ± 9.52	3.22	0.86	17.48	3.28
Temporal lobe*	25.50	7.82 ± 10.14	3.79	0.79	16.01	2.99
Amygdala	21.20	6.25 ± 9.79	3.16	0.90	25.45	3.09
Cingulate*	18.48	0.33 ± 14.42	2.58	0.77	17.65	1.85
Medial prefrontal cortex*	17.14	7.09 ± 11.68	2.37	0.67	15.33	1.69
Orbital prefrontal cortex*	14.87	18.34 ± 22.73	5.35	0.59	23.84	1.53
Parietal lobe*	14.06	4.40 ± 10.97	1.16	0.70	13.59	1.28
Dorsolateral prefrontal cortex*	13.69	10.20 ± 13.89	2.32	0.56	16.47	1.29
Raphe	12.42	16.54 ± 19.26	2.96	0.80	29.96	1.77
Occipital lobe*	9.70	8.25 ± 16.35	1.05	0.55	15.40	0.90

*Gray-matter–masked regions.
Average PD, WSMSS, ICC, %SD, and identifiability estimates are based on BP_F measurements.

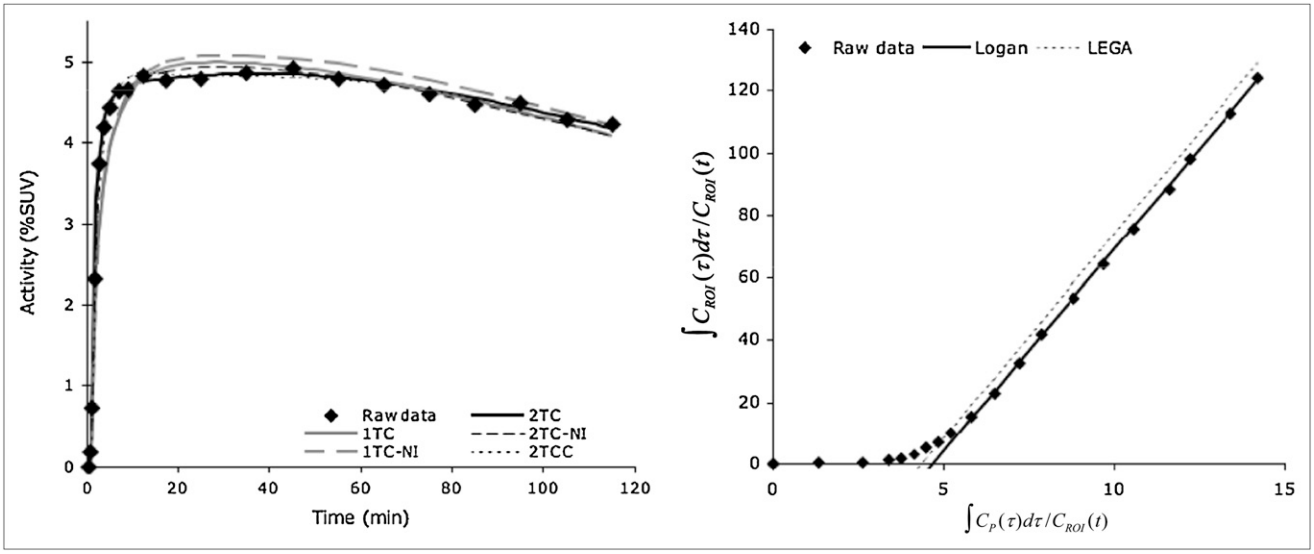

FIGURE 2. Hippocampal time–activity curve fits. On left side, 2TC (iterative, 2TC; noniterative, 2TCNI; constrained, 2TCC) model fits are indicated. Raw data are shown with diamonds. On right side, raw data are shown (♦) transformed into space used for graphical interpretation. C_p is concentration of ligand in plasma, and C_{ROI} is concentration of ligand in hippocampus. 1TC = 1 tissue compartment; 1TC-NI = 1 tissue compartment, noniterative; SUV = standardized uptake value.

Toolbox (*24*) to the target subject's brain (*25*). To calculate the probability of an ROI label for a particular voxel, the total number of transformed template ROIs assigned to that voxel was counted and divided by 18. Cortical regions were then gray-matter–masked using the target subject's segmentation. This masking was done for each ROI separately and for each voxel to establish a probabilistic set of ROIs in target subject space for use in PET analysis. For the 7 subjects, the average sizes (in cm^3) of the automatically delineated regions, from largest to smallest, were 192.5 ± 14.7 (parietal lobe), 160.1 ± 12.7 (occipital lobe), 148.8 ± 14.2 (temporal lobe), 146.5 ± 7.0 (dorsolateral prefrontal cortex), 90.2 ± 5.8 (orbital prefrontal cortex), 63.8 ± 5.8 (cerebellar gray matter), 59.5 ± 4.0 (medial prefrontal cortex), 31.7 ± 2.5 (cingulate), 21.0 ± 1.4 (insula), 18.7 ± 1.5 (hippocampus), 17.1 ± 1.6 (entorhinal cortex), 11.6 ± 0.7 (posterior parahippocampal gyrus), and 10.6 ± 0.8 (amygdala). The V_T derived from probabilistic ROIs used in this analysis was correlated with corresponding hand-drawn ROIs for ^{11}C-WAY-100635 and ^{11}C-DASB ($n = 30$; $r^2 > 0.98$).

Modeling

Modeling approaches can be divided into 2 major categories: kinetic and graphical (*14–17*). The 2-tissue-compartment (2TC) kinetic model uses a standard iterative nonlinear least squares algorithm for constrained (where the ratio of K_1/k_2 is constrained to the value of the reference region's [RR's] V_T) and unconstrained approaches. For the noniterative approach (*26*) (2TCNI), the time–activity curve is regressed on each of a library of functions. Likelihood estimation in graphical analysis (LEGA) (*27,28*) is a bias-free alternative to graphical analysis (*29*), using the last 8 time points for fitting. One-tissue-compartment and 3-tissue-compartment models proved to be unreliable and overparameterized and are not presented.

Three methods not requiring blood sampling were evaluated: the simplified reference tissue model (SRTM) (*30*) and bloodless versions of Logan analysis and LEGA. These methods used the gray matter of the cerebellum (CGM, obtained by applying an SPM5-derived gray-matter mask to the cerebellum) as an RR.

All modeling methods were applied to the time–activity curve data using a 5% blood volume correction. Weights (w_i) were assigned to each frame according to $w = \sqrt{t_i - t_{i-1}}$, where t_i is the mid-time of the current frame and t_{i-1} is the mid-time of the previous frame.

Six metrics were used to compare the models: percentage difference (PD) and within-subject mean sum of squares (WSMSS) for reproducibility, percentage SD (%SD) of BP_F, intraclass correlation coefficient (ICC) for reliability, median absolute deviation of bootstrap resampled data for identifiability, and time stability

TABLE 2
Outcome Metrics Using 120-Minute Scan and BP_F

Metric	2TC	2TCC	Logan analysis	LEGA	2TCNI
PD (%)	8.45 ± 15.17	8.32 ± 13.05	7.08 ± 14.62	7.52 ± 13.63	**6.43 ± 16.53**
WSMSS (mL/cm^3)	7.00 ± 10.54	3.85 ± 1.69	**3.32 ± 1.62**	3.36 ± 1.60	7.78 ± 7.74
ICC (unitless)	0.65 ± 0.17	0.72 ± 0.16	**0.74 ± 0.13**	**0.74 ± 0.13**	0.68 ± 0.13
SD (%)	20.45 ± 6.38	19.24 ± 4.29	19.13 ± 5.92	**18.78 ± 4.96**	22.53 ± 7.38
Identifiability (mL/cm^3)	2.73 ± 3.02	3.42 ± 3.32	2.64 ± 2.36	**2.50 ± 2.39**	3.31 ± 3.54

Mean ± SD across all subjects and all regions is shown. Models that attain best mean result in each category are in bold.

TABLE 3
Outcome Metrics Using 120-Minute Scan and BP_P

Metric	2TC	2TCC	Logan analysis	LEGA	2TCNI
PD (%)	13.22 ± 13.66	13.10 ± 11.38	11.85 ± 13.25	13.29 ± 12.37	**11.19 ± 15.16**
WSMSS (mL/cm^3)	0.81 ± 1.13	0.49 ± 0.26	**0.42 ± 0.22**	0.43 ± 0.23	0.78 ± 0.68
ICC (unitless)	0.61 ± 0.15	0.66 ± 0.16	**0.70 ± 0.11**	0.69 ± 0.11	0.65 ± 0.14
SD (%)	21.57 ± 5.98	20.15 ± 3.92	20.22 ± 5.54	**19.81 ± 4.54**	23.12 ± 6.15
Identifiability (mL/cm^3)	0.82 ± 0.94	1.02 ± 0.99	0.79 ± 0.70	**0.75 ± 0.71**	0.99 ± 1.05

Mean ± SD across all subjects and all regions is shown. Models that attain best mean result in each category are in bold.

(TS). Each of these has been described before (*14–17*), with the exception of %SD.

The %SD of an outcome measure is the SD of the sample (across experiments) divided by the sample mean.

For the RR techniques, the percentage bias was also calculated as $(100\times BP_{ND}^{\text{arterial line}} - BP_{ND}^{\text{bloodless}}/BP_{ND}^{\text{arterial line}})$, where $BP_{ND}^{\text{arterial line}}$ is the nondisplaceable binding potential (BP_{ND}) calculated using arterial input function and $BP_{ND}^{\text{bloodless}}$ is BP_{ND} calculated using the RR approach.

Voxel-Level Analysis

V_T parametric images were obtained by applying empirical Bayesian estimation in graphical analysis (EBEGA) (*31*), a fully automatic approach that incorporates LEGA (*28*) V_T estimation in a Bayesian framework. The bloodless version of the Logan method was also considered for the generation of BP_{ND} parametric images.

RESULTS

The uptake of ^{11}C-CUMI-101 is consistent with the known distribution of 5-HT_{1A}Rs (Fig. 1; Table 1).

Modeling

Figure 2 shows a representative hippocampal time–activity curve. 2TC methods fit the data well; iterative and noniterative 1-tissue-compartment models do not and are excluded from further analysis. Logan analysis and LEGA produce similar fits (Fig. 2, right).

Although the measure of interest is B_{avail}, the closest measure of receptor density that can be estimated using PET is BP_F (B_{avail}/K_D), because $1/K_D$ cannot be determined. Metric comparisons and TS analysis are performed on BP_F.

Logan analysis and LEGA are the best performers in most metrics (Table 2).

Although LEGA performs slightly better than do the other methods, the outcome metric comparisons are not strongly sensitive to model choice. Most models tested perform similarly; metric results in a single category fall within 1 SD. For all high-binding ROIs (Table 1), when BP_F estimated by 2TC methods is correlated with BP_F estimated by the LEGA approach, the slopes are close to unity (1.02, 1.02, and 1.12 for the 2TC, constrained 2TC, and 2TCNI methods, respectively), with small intercepts (−0.29, 0.26, and −1.79, respectively) and R^2 values greater than 0.90 (0.96, 0.99, and 0.95, respectively). Similar results were found when BP_F estimated by Logan analysis was regressed against LEGA results (slope = 1.00; intercept = −0.35; $R^2 > 0.99$).

For completeness, the comparisons performed in Table 2 were repeated using the ratio (at equilibrium) of specifically bound radioligand to that of total parent radioligand in plasma ($BP_P = f_P * B_{avail}/K_D$) in Table 3. Though the

TABLE 4
Metrics on High-Binding ROIs Using 120-Minute Scan and LEGA

ROI	Average VT of each ROI (mL/cm^3)	PD (%)	WSMSS (mL/cm^3)	ICC (unitless)	SD (%)	Identifiability (mL/cm^3)
Entorhinal cortex	15.41	5.57 ± 8.75	1.09	0.83	15.78	1.85
Hippocampus	15.17	7.28 ± 3.89	0.77	0.87	15.28	1.88
Insula	14.25	6.23 ± 5.28	0.65	0.77	11.45	1.52
Posterior parahippocampal gyrus	13.53	4.32 ± 4.81	0.41	0.90	14.68	1.49
Temporal lobe	13.36	7.22 ± 6.27	0.73	0.79	13.48	1.36
Amygdala	12.03	6.1 ± 4.95	0.45	0.90	17.45	1.41
Cingulate	11.27	2.87 ± 5.47	0.22	0.92	14.00	1.05
Medial prefrontal cortex	10.87	5.71 ± 5.42	0.35	0.82	12.42	1.00
Orbital prefrontal cortex	10.21	9.05 ± 7.20	0.60	0.72	13.84	0.94
Parietal lobe	9.95	4.05 ± 4.51	0.17	0.88	11.41	0.86
Dorsolateral prefrontal cortex	9.85	6.31 ± 5.72	0.33	0.79	12.37	0.87
Raphe	9.49	7.33 ± 7.59	0.40	0.83	15.66	0.94
Occipital lobe	8.65	4.44 ± 6.80	0.21	0.75	10.28	0.75
CGM	5.77	0.42 ± 4.80	0.04	0.92	11.56	0.48

TABLE 5
Average and SD of Kinetic Rate Constants Using 120-Minute Scan and 2-TC Noniterative Method

ROI	K_1	k_2	k_3	k_4
Entorhinal cortex	0.31 ± 0.18	0.08 ± 0.11	0.09 ± 0.10	0.03 ± 0.02
Hippocampus	0.34 ± 0.20	0.12 ± 0.11	0.13 ± 0.10	0.03 ± 0.01
Insula	0.39 ± 0.17	0.11 ± 0.08	0.12 ± 0.09	0.04 ± 0.02
Posterior parahippocampal gyrus	0.34 ± 0.16	0.08 ± 0.08	0.08 ± 0.07	0.04 ± 0.02
Temporal lobe	0.40 ± 0.24	0.10 ± 0.10	0.10 ± 0.06	0.05 ± 0.02
Amygdala	0.30 ± 0.17	0.07 ± 0.08	0.07 ± 0.09	0.03 ± 0.02
Cingulate	0.41 ± 0.19	0.11 ± 0.08	0.09 ± 0.05	0.05 ± 0.02
Medial prefrontal cortex	0.42 ± 0.20	0.10 ± 0.07	0.09 ± 0.06	0.06 ± 0.03
Orbital prefrontal cortex	0.39 ± 0.20	0.10 ± 0.09	0.08 ± 0.07	0.05 ± 0.02
Parietal lobe	0.44 ± 0.22	0.13 ± 0.10	0.10 ± 0.07	0.06 ± 0.02
Dorsolateral prefrontal cortex	0.41 ± 0.19	0.11 ± 0.08	0.09 ± 0.07	0.06 ± 0.02
Raphe	0.34 ± 0.21	0.11 ± 0.10	0.07 ± 0.08	0.04 ± 0.02
Occipital lobe	0.45 ± 0.23	0.15 ± 0.10	0.08 ± 0.06	0.05 ± 0.02
CGM	0.42 ± 0.22	0.15 ± 0.10	0.05 ± 0.03	0.05 ± 0.02

metrics are different, the relative performance of each of the models is similar.

Table 2 shows average metrics across all subjects and all ROIs. However, B_{avail}, hence required scan duration, may vary with each ROI (Table 1).

Most ROIs achieve less than 10% difference between test and retest, on average, and the lower-binding ROIs generally attain lower WSMSS and lower average identifiability values than the higher-binding ROIs (Table 1).

Because both free fraction and binding in the RR will affect the estimation of BP_F, outcome measures and metrics calculated using V_T (Table 4) are presented.

Rate constants are important for assessing ligand kinetics and are presented in Table 5.

Time Stability

TS was analyzed to determine the optimal scan duration. In aggregate, BP_F was not stable before 110 min (Fig. 3).

In several ROIs, BP_F values calculated using 110 min of scan data were within ±5% of those calculated using the full 120 min of data (Table 6). For other ROIs, 71% or more of the studies yielded stable BP_F values at 110 min of scan time. The TS analysis was also repeated for V_T. Except for 3 ROIs, V_T values were stable at 110 min of scan time, suggesting that shorter scans may be possible, depending on the application and the target ROI. V_T values converge faster than BP_F values (Table 6). On average, V_T values were within 8% of their terminal values from 70 min.

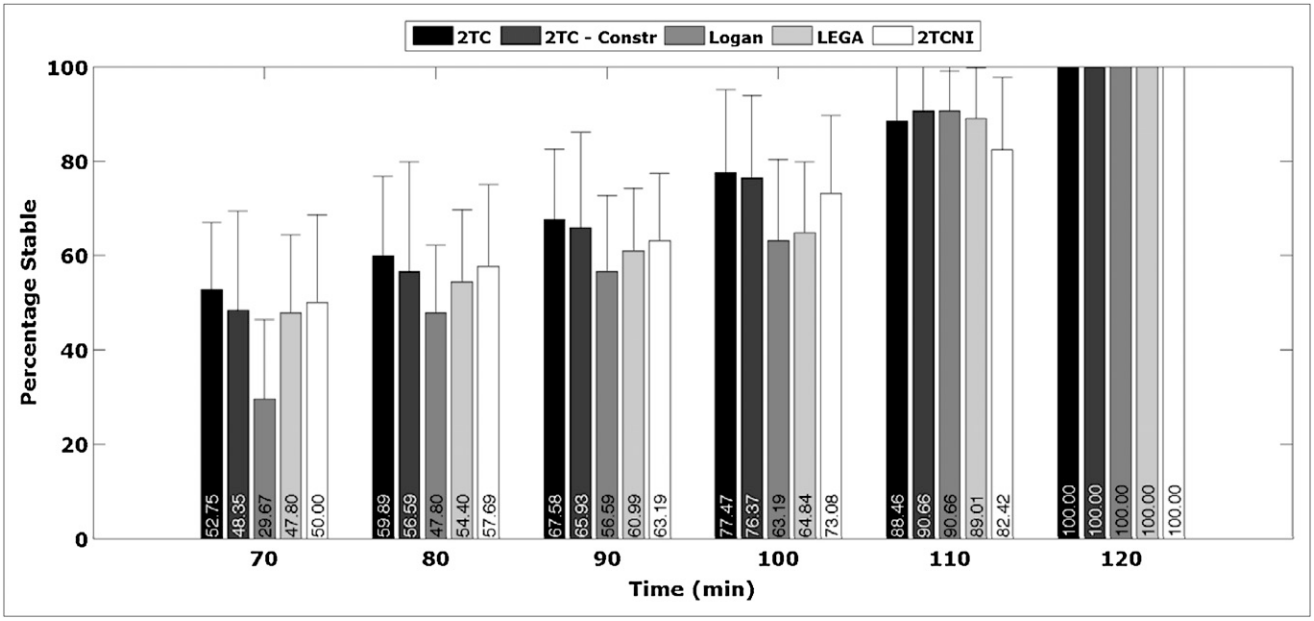

FIGURE 3. BP_F TS. BP_F was calculated using 5 models at 6 scan durations. For each region, percentage of total scans (n = 14) in which calculated BP_F was within 5% of BP_F calculated at 120 min was determined. This plot shows average of these percentages over all regions tested. Error bars indicate SD. Constr = constrained.

TABLE 6
Time–Stability Analysis of High-Binding ROIs Using LEGA

ROI	Scan length (min)											
	70		80		90		100		110		120	
	BP_F	V_T	BP_F	V_T	BP_F	V_T	BP_F	V_T	BP_F	V_T	BP_F	V_T
Entorhinal cortex	36	50	50	57	43	71	50	64	86	86	100	100
Hippocampus	29	43	57	64	57	64	57	71	79	100	100	100
Insula	43	43	57	71	86	86	86	86	100	100	100	100
Posterior parahippocampal gyrus	36	29	50	64	57	71	64	79	79	93	100	100
Temporal lobe	50	64	43	57	64	71	71	86	93	100	100	100
Amygdala	36	50	43	57	43	71	43	71	79	93	100	100
Cingulate	64	64	57	79	71	86	71	100	100	100	100	100
Medial prefrontal cortex	64	64	71	71	71	79	71	100	100	100	100	100
Orbital prefrontal cortex	50	57	50	79	57	71	57	86	79	100	100	100
Parietal lobe	79	79	86	93	79	100	93	100	100	100	100	100
Dorsolateral prefrontal cortex	64	64	64	79	64	79	71	100	100	100	100	100
Raphe	21	36	21	64	50	79	43	71	71	100	100	100
Occipital lobe	50	64	57	93	50	93	64	93	93	100	100	100

For each region, percentages of BP_F or V_T (of 14 PET scans) are indicated; values are estimated using indicated scan lengths, which fall within ±5% of BP_F or V_T values estimated using 120-min scan.

RR Approaches

The 3 RR models produce BP_{ND} values lower than those from LEGA with a plasma input function (Fig. 4). Slopes of the regression lines predicting bloodless model outcomes from those calculated using LEGA with plasma input are 0.81, 0.86, and 0.92 for bloodless versions of Logan analysis and LEGA and SRTM, respectively. The intercepts range from 0.04 to 0.11.

The mean PD over all high-binding ROIs yields similar results across RR approaches using BP_{ND} (Table 7). However, SRTM was the best performer in almost all metrics.

The TS was also analyzed using RR approaches. At 110 min of scan time, 95.05% ± 8.93% of the SRTM results were stable, on average. Bloodless Logan analysis and LEGA results at 110 min were both less than 80% stable. When SRTM BP_{ND} values at 110 min were regressed against BP_{ND} values calculated using LEGA and 120 min of scan time, the results were similar to those in Figure 4 (slope = 0.91, intercept = 0.05, and R^2 = 0.99). Metric comparisons calculated using SRTM at 110 min did not vary greatly from those presented for SRTM (with 120 min) in Table 7 (9.98% ± 11.82%, 0.008 ± 0.003, 0.64 ± 0.16, 15.57% ± 5.60%, and −3.83% ± 4.56% for mean PD, WSMSS, ICC, percentage SD, and percentage bias, respectively).

Voxel Analysis

Modeling kinetic parameters on a voxel level, as opposed to an ROI level, provides greater spatial resolution. On an ROI level, LEGA has been proven to be a reliable modeling method. However, on voxel level, the added variance results in noisy outcome measure estimates. Thus, EBEGA was applied on a voxel level (*31*). Similarly, although SRTM was found to be the optimal RR approach for ROI analysis, on a voxel level it was computationally expensive and pro-

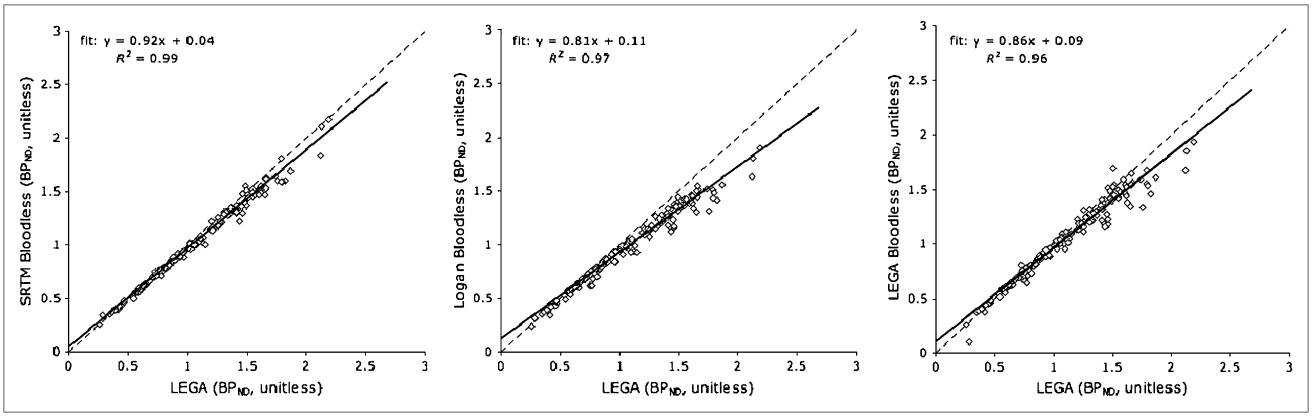

FIGURE 4. LEGA BP_{ND} with plasma input, compared with BP_{ND} values calculated by RR approaches. All high-binding ROIs listed in Table 1 are included. Identity lines are plotted (dashed lines) for reference.

TABLE 7
Metrics for Bloodless Models Using 120-Minute Scan and BP_{ND}

Metric	SRTM	Bloodless Logan analysis	Bloodless LEGA
PD (%)	**9.67 ± 11.63**	10.47 ± 11.38	11.59 ± 17.35
WSMSS (unitless)	0.008 ± 0.003	**0.007 ± 0.003**	0.010 ± 0.006
ICC (unitless)	**0.65 ± 0.13**	0.59 ± 0.16	0.56 ± 0.16
SD (%)	**15.68 ± 5.44**	14.93 ± 5.74	15.75 ± 6.50
Mean % bias	**−3.47 ± 3.60**	−7.32 ± 5.86	−3.95 ± 7.31

Mean ± SD across all subjects and all regions is shown. Models that attain best average result in each category are in bold.

duced many outliers. Therefore, an RR Logan approach was applied to produce BP_{ND} images, despite its noise-dependent bias (*32*).

To determine whether these voxel-based methods could accurately estimate outcome measures, V_T (or BP_{ND}) measurements of the high-binding regions calculated using LEGA on an ROI level were compared with those averaged within an ROI from EBEGA V_T voxel images (or reference tissue Logan BP_{ND} images; Fig. 5).The voxel-based region V_T values obtained using EBEGA were generally lower than their ROI-based counterparts (slope = 0.89; R^2 = 0.93). With BP_F and BP_P, slopes were the same and the intercept was 0.79 and 0.84, respectively. The Logan voxel method resulted in BP_{ND} values that were approximately half those of their ROI counterparts (slope = 0.58; R^2 = 0.80).

DISCUSSION

The goal of this study was to identify the optimal modeling method for ^{11}C-CUMI-101 in humans. As before, in *Papio anubis* (*14*), this goal was accomplished by assessing outcome measures (BP_F or BP_{ND}) from 10 modeling approaches on test–retest data, using 6 metrics to evaluate their performance across 6 different scan durations. This analysis was performed with ROIs derived by an automated approach, using metabolite-corrected arterial input function and reference tissue methods, with both ROI- and voxel-based modeling techniques.

Model Selection

At 120 min, the LEGA approach, using BP_F or BP_P, achieved the lowest percentage SD and best identifiability while attaining values in other categories indistinguishable from those of the other models. In addition, LEGA, using BP_F, achieved the best ICC. Because BP_F is proportional to BP_P, the metric comparisons for both BP_F and BP_P are similar. The main differences are in the values of WSMSS and identifiability, which are significantly lower in the BP_P calculation because the BP_P values themselves are lower. Importantly, all the models with input functions (Table 2) performed similarly; outcome metrics were close to each other, and BP_F estimates from differing models correlated highly. More than 90% of the V_T estimates for 5 of the lower binding regions were stable after 100 min of scan time (Table 6), and average V_T values of the highest binding regions were within 8% of their 120-min values from 70 min on (Fig. 6). Therefore, it may be possible to use shorter scan durations if V_T is the outcome measure of interest.

RR Methods

Consistent with earlier findings (*33*), all the bloodless modeling approaches yielded BP_{ND} with negative bias, compared with the LEGA method with metabolite-corrected arterial input function (Table 7; Fig. 4). Among the bloodless methods, SRTM was the most highly reproducible, although the differences were small (Table 7).

The distribution volume of nondisplaceable compartment relative to total concentration of ligand in plasma (V_{ND}) of ^{11}C-CUMI-101 is higher than that of ^{11}C-WAY-100635, a commonly used antagonist 5-HT_{1A} tracer. Higher V_{ND} is important because BP_{ND}, the outcome measure of these reference tissue models, is calculated as $BP_{ND} = (V_T - V_{ND})/V_{ND}$. It has been shown that cerebellar white matter is the most appropriate RR for ^{11}C-WAY-100635 studies, because it provides the closest approximation to nonspecific

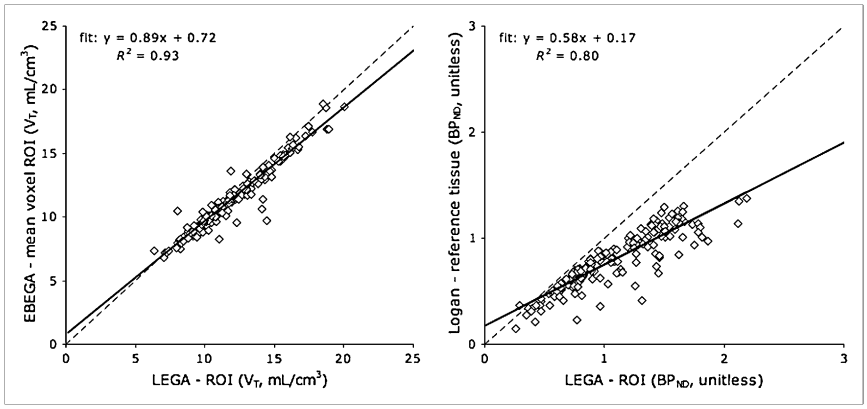

FIGURE 5. Comparison of ROI and voxel analysis. V_T (left) and BP_{ND} (right) values as found by ROI analysis vs. average of all voxels within ROI as found using voxel analysis. Identity lines are plotted (dashed lines) for reference.

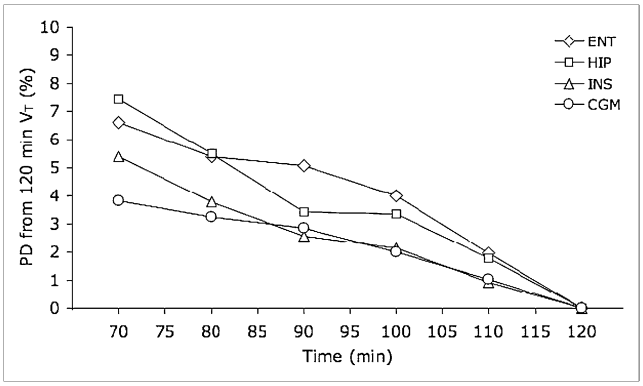

FIGURE 6. V_T TS. V_T values were calculated using LEGA and scan times ranging from 70 to 120 min. At each time period, percentage error between regional V_T at that scan duration and V_T calculated using 120 min of scan duration was calculated and averaged. Error bars are omitted for clarity. CGM = cerebellar gray matter; ENT = entorhinal cortex; HIP = hippocampus; INS = insula.

binding for that tracer (*34*). The average ^{11}C-WAY-100635 cerebellar white matter V_T is 0.29 mL/cm^3, and the average CGM V_T is 0.47 mL/cm^3. Because regional ^{11}C-WAY-100635 V_T values vary from 27.73 mL/cm^3 (in the occipital lobe) to 64.92 mL/cm^3 (in the hippocampus), BP_{ND} could be underestimated (using the CGM instead of cerebellar white matter as the RR) by approximately 38%. On the other hand, the average CGM V_T for ^{11}C-CUMI-101 is 5.77 mL/cm^3. Because ^{11}C-CUMI-101 binds only to the high-affinity 5-HT_{1A}Rs, specific binding is approximately half that of ^{11}C-WAY-100635 (0.09 mL/cm^3 in the cerebellum). Regional ^{11}C-CUMI-101 V_T varies from 8.7 mL/cm^3 (in the occipital lobe) to 15.41 mL/cm^3 (in the entorhinal cortex). Because the amount of specific binding, compared with the total binding, within the cerebellum is so low, underestimation error in these regions varies between 2.4% and 4.4%.

Voxel-Based Analysis

Voxel-based analysis is a potentially valuable method because it increases the spatial resolution of the results—an important outcome because most anatomic structures in the brain are not necessarily functionally homogeneous. The cost of this increased resolution is increased noise. On the ROI level, the LEGA approach proved to be most reliable. However, on the voxel level, LEGA does not perform well; therefore, when using an arterial input function, EBEGA was employed (*31*). EBEGA outperforms the other voxel-based methods tested in this study by yielding fewer outliers and producing the highest correlation with the least bias when compared with the winning ROI-based method.

Limitations and Other Considerations

In the current series of studies, test–retest scans were obtained on the same day from each subject. How sensitive ^{11}C-CUMI101 may be to displacement from binding by endogenous 5-HT in humans remains a question. We know from animal experiments that ^{11}C-CUMI101 can be displaced from binding by endogenous 5-HT in response to a substantial pharmacologic challenge (*35*).

It has been shown that antagonist 1A binding correlates with age, sex, lifetime aggression, and C1019G polymorphism of the 5-HT_{1A} gene promotor region (*5,36*). We have not attempted to control for these variables because they are unimportant in a within-subject comparison design such as the one presented in the current work.

In addition, the RR used in this work was the CGM. Although outcome measures calculated using this RR were highly reproducible, validating the use of the CGM as an appropriate RR will require further experiments (binding in the CGM can be evaluated before and after administration of pindolol).

For the graphical approaches, only the last 8 time points, corresponding to minutes 40 through 120, were used for the model fitting. Because the kinetic approaches use the full time series of the time–activity curve data, which contain many more data points, comparison of some outcome metrics between kinetic and graphical approaches may be somewhat unfair. This is especially true for the identifiability measure, which—in the case of the graphical approaches—is based on only 8 points and is thus a limitation of the model comparisons. However, as indicated by the similarity of outcome metrics across all modeling techniques, the results were not strongly sensitive to model choice or number of data points used. In addition, the quantitative model metric comparison was used as a guide in model selection. Model results were also visually inspected and compared.

Another possible limitation is the fact that the CGM RR could not be adequately fitted with a 1-tissue-compartment model. A cluster analysis was performed (data not shown) in an attempt to find any contiguous volume of voxels, the time–activity curve of which may be adequately fitted with a 1-tissue-compartment model. The fact that no such volume was found may be due to specific binding, partial-volume effect, radioactive metabolites in the brain (unlikely, because all metabolites are more polar), or significant, unequal nonspecific binding to 2 different targets.

CONCLUSION

Ten different modeling techniques were tested using 6 metrics and a TS analysis. In humans, at full scan duration the LEGA model yielded slightly better performance than the other methods presented. The reference tissue methods performed similarly on the metrics. When full quantification was used with arterial input function, this study indicates that a 120-min scan is advisable for the accurate estimation of BP_F.

ACKNOWLEDGMENTS

This work was supported in part by PHS grants MH62185, MH077161, and MH076258.

REFERENCES

1. Kasper S, Tauscher J, Willeit M, et al. Receptor and transporter imaging studies in schizophrenia, depression, bulimia and Tourette's disorder: implications for psychopharmacology. *World J Biol Psychiatry.* 2002;3:133–146.
2. Jolas T, Schreiber R, Laporte AM, et al. Are postsynaptic 5-HT1A receptors involved in the anxiolytic effects of 5-HT1A receptor agonists and in their inhibitory effects on the firing of serotonergic neurons in the rat? *J Pharmacol Exp Ther.* 1995;272:920–929.
3. Arango V, Underwood MD, Boldrini M, et al. Serotonin 1A receptors, serotonin transporter binding and serotonin transporter mRNA expression in the brainstem of depressed suicide victims. *Neuropsychopharmacology.* 2001;25:892–903.
4. Stanley M, Mann JJ. Increased serotonin-2 binding sites in frontal cortex of suicide victims. *Lancet.* 1983;1:214–216.
5. Parsey RV, Olvet DM, Oquendo MA, Huang YY, Ogden RT, Mann JJ. Higher 5-HT1A receptor binding potential during a major depressive episode predicts poor treatment response: preliminary data from a naturalistic study. *Neuropsychopharmacology.* 2006;31:1745–1749.
6. Parsey RV, Oquendo MA, Ogden RT, et al. Altered serotonin 1A binding in major depression: a [carbonyl-C-11]WAY100635 positron emission tomography study. *Biol Psychiatry.* 2006;59:106–113.
7. Mann JJ, McBride PA, Brown RP, et al. Relationship between central and peripheral serotonin indexes in depressed and suicidal psychiatric inpatients. *Arch Gen Psychiatry.* 1992;49:442–446.
8. Placidi GP, Oquendo MA, Malone KM, Huang YY, Ellis SP, Mann JJ. Aggressivity, suicide attempts, and depression: relationship to cerebrospinal fluid monoamine metabolite levels. *Biol Psychiatry.* 2001;50:783–791.
9. Cheney BV, Lahti RA, Barsuhn C. Drug affinities for the agonist and antagonist states of the opioid receptor. *Eur J Pharmacol.* 1982;77:259–263.
10. De Lean A, Stadel JM, Lefkowitz RJ. A ternary complex model explains the agonist-specific binding properties of the adenylate cyclase-coupled beta-adrenergic receptor. *J Biol Chem.* 1980;255:7108–7117.
11. Bantick RA, Rabiner EA, Hirani E, de Vries MH, Hume SP, Grasby PM. Occupancy of agonist drugs at the 5-HT1A receptor. *Neuropsychopharmacology.* 2004;29:847–859.
12. Narendran R, Hwang DR, Slifstein M, et al. In vivo vulnerability to competition by endogenous dopamine: comparison of the D_2 receptor agonist radiotracer (−)-*N*-[^{11}C]propyl-norapomorphine ([^{11}C]NPA) with the D_2 receptor antagonist radiotracer [^{11}C]-raclopride. *Synapse.* 2004;52:188–208.
13. Kumar JS, Prabhakaran J, Majo VJ, et al. Synthesis and in vivo evaluation of a novel 5-HT_{1A} receptor agonist radioligand [*O*-methyl-^{11}C]2-(4-(4-(2-methoxyphenyl)piperazin-1-yl)butyl)-4-methyl-1,2,4-triazi ne-3,5(2H,4H)dione in nonhuman primates. *Eur J Nucl Med Mol Imaging.* 2007;34:1050–1060.
14. Milak MS, Severance AJ, Ogden RT, et al. Modeling considerations for ^{11}C-CUMI-101, an agonist radiotracer for imaging serotonin 1A receptor in vivo with PET. *J Nucl Med.* 2008;49:587–596.
15. DeLorenzo C, Kumar JS, Zanderigo F, Mann JJ, Parsey RV. Modeling considerations for in vivo quantification of the dopamine transporter using [^{11}C]PE2I and positron emission tomography. *J Cereb Blood Flow Metab.* 2009;29:1332–1345.
16. Ogden RT, Ojha A, Erlandsson K, Oquendo MA, Mann JJ, Parsey RV. In vivo quantification of serotonin transporters using [^{11}C]DASB and positron emission tomography in humans: modeling considerations. *J Cereb Blood Flow Metab.* 2007;27:205–217.
17. Parsey RV, Slifstein M, Hwang DR, et al. Validation and reproducibility of measurement of 5-HT1A receptor parameters with [carbonyl-11C]WAY-100635 in humans: comparison of arterial and reference tissue input functions. *J Cereb Blood Flow Metab.* 2000;20:1111–1133.
18. Gunn RN, Sargent PA, Bench CJ, et al. Tracer kinetic modeling of the 5-HT1A receptor ligand [carbonyl-11C]WAY- 100635 for PET. *Neuroimage.* 1998;8:426–440.
19. DeLorenzo C, Klein A, Mikhno A, et al. A new method for assessing PET-MRI coregistration. *Proceedings of the SPIE.* 2009;7258:72592W-7–72592W-8.
20. Duvernoy H. *The Human Brain: Surface, Three-dimensional Sectional Anatomy and MRI*. New York, NY: Springer-Verlag Wien; 1991.
21. Talairach J, Tournoux P. *Co-Planar Stereotactic Atlas of the Human Brain: Three-Dimensional Proportional System—An Approach of Cerebral Imaging*. New York, NY: Theime Medical Publisher; 1988.
22. Kates WR, Abrams MT, Kaufmann WE, Breiter SN, Reiss AL. Reliability and validity of MRI measurement of the amygdala and hippocampus in children with fragile X syndrome. *Psychiatry Res Neuroimaging.* 1997;75:31–48.
23. Killiany RJ, Moss MB, Nicholson T, Jolesz F, Sandor T. An interactive procedure for extracting features of the brain from magnetic resonance images: the lobes. *Hum Brain Mapp.* 1997;5:355–363.
24. Ardekani BA, Guckemus S, Bachman A, Hoptman MJ, Wojtaszek M, Nierenberg J. Quantitative comparison of algorithms for inter-subject registration of 3D volumetric brain MRI scans. *J Neurosci Methods.* 2005;142:67–76.
25. Klein A, Andersson J, Ardekani BA, et al. Evaluation of 14 nonlinear deformation algorithms applied to human brain MRI registration. *Neuroimage.* 2009; 46:786–802.
26. Simpson HB, Lombardo I, Slifstein M, et al. Serotonin transporters in obsessive-compulsive disorder: a positron emission tomography study with [^{11}C]McN 5652. *Biol Psychiatry.* 2003;54:1414–1421.
27. Parsey RV, Ogden RT, Mann JJ. Determination of volume of distribution using likelihood estimation in graphical analysis: elimination of estimation bias. *J Cereb Blood Flow Metab.* 2003;23:1471–1478.
28. Ogden RT. Estimation of kinetic parameters in graphical analysis of PET imaging data. *Stat Med.* 2003;22:3557–3568.
29. Logan J, Fowler JS, Volkow ND, et al. Graphical analysis of reversible radioligand binding from time-activity measurements applied to [*N*-^{11}C-methyl]-(−)-cocaine PET studies in human subjects. *J Cereb Blood Flow Metab.* 1990;10:740–747.
30. Lammertsma AA, Hume SP. Simplified reference tissue model for PET receptor studies. *Neuroimage.* 1996;4:153–158.
31. Zanderigo F, Ogden RT, Bertoldo A, Cobelli C, Mann JJ, Parsey RV. Empirical Bayesian estimation in graphical analysis: a voxel-based approach for the determination of the volume of distribution in PET studies. *Nucl Med Biol.* 2010;37:443–451.
32. Slifstein M, Laruelle M. Effects of statistical noise on graphic analysis of PET neuroreceptor studies. *J Nucl Med.* 2000;41:2083–2088.
33. Hirvonen J, Johansson J, Teras M, et al. Measurement of striatal and extrastriatal dopamine transporter binding with high-resolution PET and [^{11}C]PE2I: quantitative modeling and test-retest reproducibility. *J Cereb Blood Flow Metab.* 2008;28:1059–1069.
34. Parsey RV, Ogden RT, Miller JM, et al. Higher serotonin 1A binding in a second major depression cohort: modeling and reference region considerations. *Biol Psychiatry.* 2010;68:170–178.
35. Milak MS, Kumar JSD, Severance AJ, et al. Altered binding in baboons of [C-11]CUMI-101, a 5-HT1A agonist PET tracer, in response to intravenous citalopram. *Neuroimage.* 2008;41:T162–T162.
36. Parsey RV, Oquendo MA, Simpson NR, et al. Effects of sex, age, and aggressive traits in man on brain serotonin 5-HT1A receptor binding potential measured by PET using [C-11]WAY-100635. *Brain Res.* 2002;954:173–182.